Rock and Soil Mechanics

Volume 44 | Issue 2 Article 9

4-10-2023

# P-wave velocity tomography and acoustic emission characteristics of sandstone under uniaxial compression

Guang ZHANG
*Faculty of Land Resources Engineering, Kunming University of Science and Technology, Kunming, Yunnan 650093, China*

Shun-chuan WU
*Faculty of Land Resources Engineering, Kunming University of Science and Technology, Kunming, Yunnan 650093, China, Key Laboratory of Ministry of Education for Efficient Mining and Safety of Metal Mine, University of Science and Technology Beijing, Beijing 100083, China, Key Laboratory of Geohazard Forecast and Geoecological Restoration in Plateau Mountainous Area, Ministry of Natural Resources of the People's Republic of China, Kunming University of Science and Technology, Kunming, Yunnan 650093, China*

Shi-huai ZHANG
*Department of Earth Sciences, ETH Zürich, Zürich, Switzerland 8092*

Pei GUO
*Key Laboratory of Ministry of Education for Efficient Mining and Safety of Metal Mine, University of Science and Technology Beijing, Beijing 100083, China*



## Recommended Citation

ZHANG, Guang; WU, Shun-chuan; ZHANG, Shi-huai; and GUO, Pei (2023) "P-wave velocity tomography and acoustic emission characteristics of sandstone under uniaxial compression," *Rock and Soil Mechanics*: Vol. 44: Iss. 2, Article 9.
DOI: 10.16285/j.rsm.2022.6106
Available at: https://rocksoilmech.researchcommons.org/journal/vol44/iss2/9

Rock and Soil Mechanics 2023 44(2): 483–496 ISSN 1000–7598
https: //doi.org/10.16285/j.rsm.2022.6106 http://rocksoilmech.researchcommons.org/journal

# P-wave velocity tomography and acoustic emission characteristics of sandstone under uniaxial compression

ZHANG Guang[1], WU Shun-chuan[1, 2, 3], ZHANG Shi-huai[4], GUO Pei[2]

1. Faculty of Land Resources Engineering, Kunming University of Science and Technology, Kunming, Yunnan 650093, China
2. Key Laboratory of Ministry of Education for Efficient Mining and Safety of Metal Mine, University of Science and Technology Beijing, Beijing 100083, China
3. Key Laboratory of Geohazard Forecast and Geoecological Restoration in Plateau Mountainous Area, Ministry of Natural Resources of the People's Republic of China, Kunming University of Science and Technology, Kunming, Yunnan 650093, China
4. Department of Earth Sciences, ETH Zürich, Zürich, Switzerland 8092

**Abstract:** Pillar burst is one of the most frequent dynamic disasters in deep mining, which poses a serious threat to safe and efficient mining. In this study, the failure mechanisms and precursors of pillar burst are investigated by active ultrasonic survey and passive acoustic emission (AE) monitoring in uniaxial compression tests on Zigong red sandstone. Combining active and passive AE monitoring data, a P-wave velocity tomography inversion is performed to analyse the temporal and spatial variations of P-wave velocity structure during the sample failure. Results show that the velocity structure of the sandstone sample is highly heterogeneous during loading, and a low-velocity zone emerges, within which most of the acoustic emission events are present. The dispersion of P-wave velocity reflects the global variations of P-wave velocity. It changes drastically during the peak stage, and increases with the ongoing loading. The AE events differ significantly between the pre-peak and post-peak stages. In the pre-peak stage, AE events are randomly distributed in the sample, while in the post-peak stage, clustered AE events are identified. In addition, it is found that using the homogeneous velocity structure for AE events location results in a higher positioning error. The decreasing *b* value before the eventual failure of the sample indicates that large-scale crack activities are intensified, leading to the increase of sample heterogeneity, which also proves the necessity of applying the heterogeneous velocity structure for AE events location. The research results can be further used for on-site pillar stability monitoring, and the periodic P-wave velocity tomography provides precursors for pillar bursts.
**Keywords:** acoustic emission; ultrasonic wave; tomography; pillar burst; uniaxial compression

## 1 Inroduction

With the depletion of shallow resources, exploitation of resources continues to advance to the deep, and deep mining of mineral resources larger than 1 km becomes normal. Deep stopes and roadways are commonly located in complex geological environments with high in situ stresses, and they are prone to rockburst disasters. The occurrence of rockburst disasters is sudden, random and destructive, and often causes heavy casualty and serious economic loss.

Pillar instability failure, as a common rockburst disaster form, mainly includes two categories: pillar progressive failure and pillar burst. Figure 1 shows the mechanical model of stable failure (progressive failure) and unstable failure (pillar burst) after the pillar reaches the peak load. Pillar stability depends on the relationship between pillar stiffness and surrounding rock stiffness. In Fig. 1, $K_p$ and $K_m$ represent the stiffnesses of pillar and surrounding rock, respectively. When $K_p < K_m$, the fracture energy required by pillar after peak load is greater than the elastic energy accumulated at the peak. At this time, it still needs to apply load to maintain progressive failure, thus it can be considered to be in stable failure state. When $K_p > K_m$, the fracture energy required after peak load is less than the elastic energy accumulated at the peak, and the fracture will expand without additional load. In this case, the system composed of pillar and surrounding rock is in an unstable failure state, causing pillar burst[1–4]. The instability of a single pillar will cause overload of surrounding pillars, leading to chain instability and large-scale instability events of pillar groups, and then seriously threatening personnel, equipment and production safety[5–6].

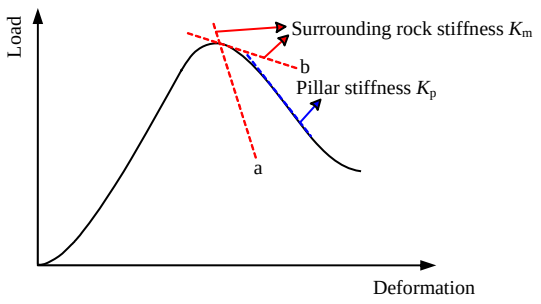


**Fig. 1 Illustration of stable and unstable post-failure behavior in pillars[2–3]**

Received: 15 July 2022 Accepted: 31 October 2022
This work was supported by the National Natural Science Foundation of China (51934003), the Major Science and Technology Special Project of Yunnan Province (202102AG050024) and the Yunnan High Level Talent Introduction Plan "High Level Innovation and Entrepreneurship Team".
First author: ZHANG Guang, male, born in 1992, PhD candidate, mainly engaged in rock mechanics test and acoustic emission monitoring research.
E-mail: zhangguang09@163.com
Corresponding author: WU Shun-chuan, male, born in 1969, PhD, Professor, Doctoral supervisor, mainly engaged in the teaching and research of geotechnical engineering and mining engineering. E-mail：wushunchuan@ ustb.edu.cn

Laboratory test is an effective means to study pillar burst[7]. In situ pillar can be simplified as a sample subjected to the load from surrounding rocks. Based on the laboratory research on pillar failure, major factors affecting pillar stability are summarized as follows: the pillar width-to-height ratio, and the stiffness ratio of loading system to pillar[8−10]. In the study of rock failure, monitoring approaches such as stress, acoustic emission (AE), thermal infrared imaging, computed tomography (CT) and digital image correlation (DIC)[11−13] have been widely used. He et al.[14] employed the rockburst test system to study the failure process of pillar burst. The evolution of pillar burst damage was investigated by high-speed photography, AE and fractal dimension. Through true triaxial test, Chen et al.[15] found that thermal infrared temperature and AE count could provide early warning of rock failure.

The initiation and propagation of microcracks in rock not only produce AE events, but also lead to the changes in wave velocity. As an effective nondestructive testing method, ultrasonic testing has been extensively adopted by many scholars to study the relationship between wave velocity and rock damage. Goodfellow et al.[16] used active and passive ultrasonic technology to study P-wave velocity attenuation characteristics during sandstone damage. Yukutake[17] found that the change of wave velocity was related to the formation and evolution of fracture zone. Meglis et al.[18] studied the tunnel excavation damage in the underground laboratory of Atomic Energy of Canada Limited (AECL) through ultrasonic measurement and found that the wave velocity was the highest in compressive stress concentration zone on the side wall of roadway and the lowest in tensile stress concentration zone. Great progress has been made in rock damage research by using active ultrasonic testing to obtain wave velocity changes in specific paths or tomography based on ultrasonic measurement data[19−20]. However, both ultrasonic wave velocity path and ultrasonic tomography range are limited by the number of sensors. It is difficult for a limited number of sensors to completely cover the sample to be tested or the detected area, which may result in the omission of information in key areas of concern. Zhang et al.[4] adopted the active ultrasonic technology in the uniaxial compression test on Zigong sandstone to build a wave velocity model that varies with time. However, due to the limitation of the number of sensors deployed, the detected area was not satisfactorily covered. Brantut[21] proposed a wave velocity tomography method containing active and passive data, which can make full use of fracture-induced AE events to enhance path coverage to build a more effective three-dimensional (3D) velocity model. The proposed model replaced the uniform velocity model with velocity inversion model so as to improve the AE events location accuracy, which has addressed the limitation of ray path of conventional ultrasonic tomography.

In this paper, the uniaxial compression test is conducted on sandstone to study the pillar burst. The ultrasonic test and AE monitoring data are collected to analyze the failure process. Moreover, the FaATSO method[21] combined with active (ultrasonic testing) and passive (AE monitoring) data inversion is used to explore the change of wave velocity. The evolution of wave velocity during failure is then analyzed, and the wave velocity inversion model is applied to the AE event location to improve the location accuracy.

## 2 Wave velocity tomography method based on integrated inversion

In the field of seismicity, tomography is used to determine the local inhomogeneity and fine structure of rock mass in the earth. In the field of rock mechanics, the internal wave velocity field of samples can be derived by observing waveform information, providing an insight into the internal fracture and stress inhomogeneity information. Travel time tomography can be divided into two stages: forward modeling and inversion modeling. Forward modeling acquires the ray path and travel time between the source and sensors by solving the eikonal equation. Inversion modeling searches optimal solutions by solving a series of linear or nonlinear optimization problems.

### 2.1 Eikonal equation

Eikonal equation in two-dimensional (2D) anisotropic medium is expressed as[22−23]:

$$\sqrt{\left(\frac{\partial u}{\partial x}\right)^2+\left(\frac{\partial u}{\partial z}\right)^2}\times V\left(\frac{\nabla u}{|\nabla u|}\right)=1 \tag{1}$$

where $u(x,z)$ is the arrival time of wave front at point ($x$, $z$) in 2D medium (s); $V(x,z)$ is the wave velocity (m/s); and ($x$, $z$) is the 2D plane coordinate system (m).

In 3D case, the eikonal equation in anisotropic medium is written by

$$\sqrt{\left(\frac{\partial u}{\partial x}\right)^2+\left(\frac{\partial u}{\partial y}\right)^2+\left(\frac{\partial u}{\partial z}\right)^2}\times V\left(\frac{\nabla u}{|\nabla u|}\right)=1 \tag{2}$$

where $u(x, y, z)$ is the arrival time of wave front at point ($x$, $y$, $z$) in 3D medium (in s); $V(x, y, z)$ is the wave velocity (m/s); and ($x$, $y$, $z$) is the 3D plane coordinate system (m).

### 2.2 Fast marching method

Fast marching method (FMM) is an effective discretization method to solve eikonal equation. The cores of FMM are upwind difference and narrow band technology[24]. The upwind difference is used to calculate local travel time by solving the eikonal equation. The narrow band technology is aimed at simulating wave front propagation and calculation of global travel time[25−26].

2.2.1 Principle of local travel time calculation

In 2D case, elastic wave travel time $u(x, z)$ is a function of space coordinate ($x$, $z$), and its first-order partial differential operator in $x$ and $z$ directions are $\partial u/\partial x$ and $\partial u/\partial z$. In numerical calculation, the partial differential is approximated by difference, and

the upwind difference operator is derived by Taylor expansion. The discrete eikonal equation of upwind scheme is expressed as follows:

$$\left\{\max\left(D_{ij}^{-x}u,-D_{ij}^{+x}u,0\right)^2+\max\left(D_{ij}^{-z}u,-D_{ij}^{+z}u,0\right)^2\right\}^{1/2}\times V_{ij}(\theta)=1 \tag{3}$$

where $D_{ij}^{-x}u$ and $D_{ij}^{-z}u$ are the first-order forward difference operators in $x$ and $z$ directions; $D_{ij}^{+x}u$ and $D_{ij}^{+z}u$ are the first-order backward difference operators in $x$ and $z$ directions; and $V_{ij}(\theta)$ is the wave velocity of point $(i, j)$ along the angle $\theta$ with $x$ direction (m/s).

The travel time of 2D space point ($i$, $j$) is known, and the grid node layout is shown in Fig. 2(a). Based on the known travel time points, the travel time of adjacent points can be calculated. The first-order forward and backward difference operators of travel time function $u$ in $x$ and $z$ directions are

$$\left.\begin{aligned}D_{ij}^{-x}u&=\frac{u_{i,j}-u_{i-1,j}}{\Delta x},\ D_{ij}^{+x}u=\frac{u_{i+1,j}-u_{i,j}}{\Delta x}\\ D_{ij}^{-z}u&=\frac{u_{i,j}-u_{i,j-1}}{\Delta z},\ D_{ij}^{+z}u=\frac{u_{i,j+1}-u_{i,j}}{\Delta z}\end{aligned}\right\} \tag{4}$$

The points ($i$, $j$), ($i$+1, $j$) and ($i$+1, $j$) are taken for examples, and their locations are given in Fig. 2(a). Suppose that the travel times of points ($i$+1, $j$) and ($i$+1, $j$) have been calculated, and the travel time of point ($i$, $j$) needs to be calculated or updated. Point ($i$, $j$) satisfies the first-order backward difference scheme (Eq. (4)) in $x$ and $z$ directions, then we have

$$\left.\begin{aligned}D_{ij}^{+x}u&=\frac{u_{i+1,j}-u_{i,j}}{\Delta x}\\ D_{ij}^{+z}u&=\frac{u_{i,j+1}-u_{i,j}}{\Delta z}\end{aligned}\right\} \tag{5}$$

By substituting Eq. (5) into eikonal equation Eq. (3), we can obtain

$$\left(\frac{u_{i+1,j}-u_{i,j}}{\Delta x}\right)^2+\left(\frac{u_{i,j+1}-u_{i,j}}{\Delta z}\right)^2=s_{i,j}^2 \tag{6}$$

where $s_{i,j}$ is the slowness, and $s_{i,j}=1/V_{i,j}$.

For square grids, i.e. grid spacing $h=\Delta x=\Delta z$, the first-order difference operator of travel time $u_{i,j}$ calculated from the four points (($i$±1, $j$), ($i$, $j$±1)) around the point ($i$, $j$) is as follows:

$$\left.\begin{aligned}u_{i,j}&=\frac{u_{i\pm1,j}+u_{i,j\pm1}+\sqrt{2\left(s_{i,j}h\right)^2-\left(u_{i\pm1,j}-u_{i,j\pm1}\right)^2}}{2}\\ u_{i,j}&=u_{i\pm1,j}+s_{i,j}h\\ u_{i,j}&=u_{i,j\pm1}+s_{i,j}h\end{aligned}\right\} \tag{7}$$

The travel time of point ($i$, $j$) cannot be calculated by the travel time of four surrounding points at the same time. Hence, the formula satisfying the updating conditions in Eq. (7) in the direction of narrow band expansion should be selected to calculate the travel time at point ($i$, $j$), and then the minimum of multiple solutions should be taken as the travel time at point ($i$, $j$).

The above results are first-order difference operators and arrival time calculation of upwind difference scheme in 2D coordinate system. Similarly, the second-order difference operators and arrival time calculation results can be deduced (Fig. 2(b)):

$$\left.\begin{aligned}D_{i,j}^{\pm2x}u&=-\frac{3u_{i,j}-4u_{i\pm1,j}+u_{i\pm2,j}}{2\Delta x}\\ D_{i,j}^{\pm2z}u&=-\frac{3u_{i,j}-4u_{i,j\pm1}+u_{i,j\pm2}}{2\Delta z}\end{aligned}\right\} \tag{8}$$

Thereby, the second-order difference scheme calculation formula of travel time $u_{i,j}$ at point to be solved ($i$, $j$) constructed by eight surrounding points is

$$\left.\begin{aligned}u_{i,j}&=\frac{\left(4u_{i\pm1,j}-u_{i\pm2,j}\right)+\left(4u_{i,j\pm1}-u_{i,j\pm2}\right)+\sqrt{8\left(s_{i,j}h\right)^2-\left[\left(4u_{i\pm1,j}-u_{i+2,j}\right)-\left(4u_{i,j\pm1}-u_{i,j\pm2}\right)\right]^2}}{6}\\ u_{i,j}&=\frac{3\left(4u_{i\pm1,j}-u_{i\pm2,j}\right)+4u_{i,j\pm1}+2\sqrt{13\left(s_{i,j}h\right)^2-\left(4u_{i\pm1,j}-u_{i\pm2,j}-3u_{i,j\pm1}\right)^2}}{13}\\ u_{i,j}&=\frac{3\left(4u_{i,j\pm1}-u_{i,j\pm2}\right)+4u_{i\pm1,j}+2\sqrt{13\left(s_{i,j}h\right)^2-\left(4u_{i,j\pm1}-u_{i,j\pm2}-3u_{i\pm1,j}\right)^2}}{13}\\ u_{i,j}&=\frac{u_{i\pm1,j}+u_{i,j\pm1}+\sqrt{2\left(s_{i,j}h\right)^2-\left(u_{i\pm1,j}-u_{i,j\pm1}\right)^2}}{2}\\ u_{i,j}&=u_{i\pm1,j}+s_{i,j}h\\ u_{i,j}&=u_{i,j\pm1}+s_{i,j}h\end{aligned}\right\} \tag{9}$$

Note that the second-order difference operators cannot be applied globally, and the components where the second-order difference operators are not applicable at boundaries or corner need to be converted into first-order difference operators to guarantee stable global solutions[21].

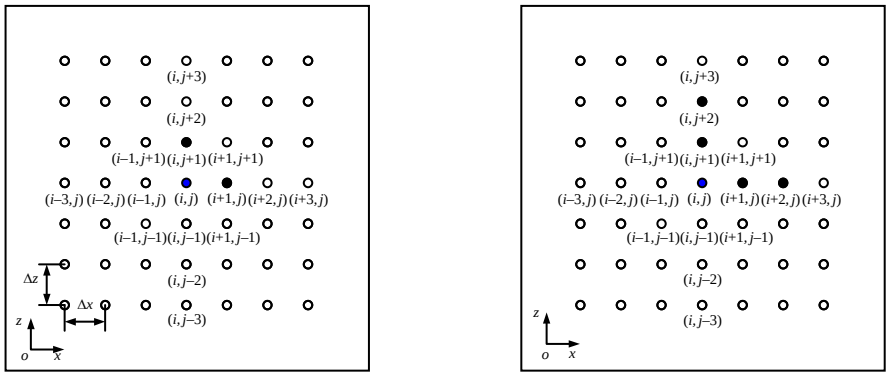


(a) Calculation of first-order difference operators (b) Calculation of second-order difference operators

**Fig. 2 Discrete mesh schematic diagrams of the upwind difference scheme**

2.2.2 Implementation of travel time calculation

As a grid-based ray tracing method, FMM uses narrow band extension to obtain the travel time of wave front in global grid nodes[27−30]. Figure 3 illustrates the narrow band extension principle on a 2D plane. All grid nodes can be divided into three regions: upwind, narrow band, and downwind. Upwind region is composed of grid nodes behind the wave front, narrow band region is composed of grid nodes on the wave front, and downwind region contains points ahead of the wave front. The points in upwind region are known as the known points that have completed the travel time calculation. The points located in the narrow band region are called trial points. Their travel times are calculated by the adjacent known points. The points located in the downwind region are called unknown points. The calculation of travel time has not been performed at unknown points yet. The specific procedure of narrow band method is described as follows:

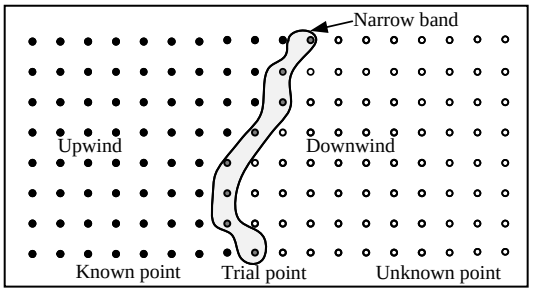


**Fig. 3 Principle of the narrow band method (after Sethian et al.[27])**

(1) Discretize the calculation area and assign corresponding slowness $s_{i,j}$ to the grid nodes.

(2) Set the source point as the known point, whose travel time $u$ is equal to 0.

(3) The four nodes adjacent to the known point are set as trial points (if they are known points, they remain unchanged), and the travel time of trial point is calculated respectively according to Eq. (7) or Eq. (9). The remaining nodes are set as unknown points, whose travel times are infinity.

(4) Modify the trial points attribute of minimum travel time to known points. If the adjacent point is an unknown point, modify its attribute to trial point. If the adjacent point is a known point, it will not be considered in the calculation.

(5) Check whether the narrow band is empty. If there are still trial points, repeat steps (3) and (4) until the travel time calculations of all nodes are done.

### 2.3 Tomographic inversion algorithm of first-arrival travel time

The purpose of tomographic inversion is to interpret the physical state inside the rock model using the AE monitoring data. The tomographic inversion can be summarized as the solving of eikonal equation:

$$\boldsymbol{d} = \boldsymbol{g}(\boldsymbol{m}) \tag{10}$$

where $\boldsymbol{d}$ is the observation data obtained from the test, including the arrival time information of active events and passive events; $\boldsymbol{m}$ is the model parameter, including model wave velocity, anisotropic parameter and AE event coordinates; and $\boldsymbol{g}$ is the eikonal equation operator.

The tomographic inversion of the first-arrival travel time is to adjust the model parameter matrix $\boldsymbol{m}$ and update the travel time of active/passive waveform information to match the observation data through forward algorithm[24, 31]. FaATSO program uses pseudo-Newton method[32] to construct model parameter matrix during inversion. In the pseudo-Newton method, minimization is achieved by iteration. The updating steps of model parameter $\boldsymbol{m}$ are given as follows:

$$\begin{aligned}\boldsymbol{m}_{n+1} = \boldsymbol{m}_n - \mu_n \left(\boldsymbol{G}_n^t \boldsymbol{C}_{\mathrm{D}}^{-1} \boldsymbol{G}_n + \boldsymbol{C}_{\mathrm{M}}^{-1}\right)^{-1} \left[\boldsymbol{G}_n^t \boldsymbol{C}_{\mathrm{D}}^{-1} \cdot \right. \\ \left. \left(\boldsymbol{d}_n - \boldsymbol{d}_{\mathrm{obs}}\right) + \boldsymbol{C}_{\mathrm{M}}^{-1} \left(\boldsymbol{m}_n - \boldsymbol{m}_{\mathrm{prior}}\right)\right]\end{aligned} \tag{11}$$

where $\boldsymbol{m}_{\mathrm{prior}}$ is a priori model parameter; $\boldsymbol{m}_{n+1}$ and $\boldsymbol{m}_n$ are the model parameters at iterative steps $n$+1 and $n$, respectively; $\boldsymbol{d}_n$ is the observation data at iterative step $n$; $\boldsymbol{d}_{\mathrm{obs}}$ is the observation dataset; $\mu_n$ is the iteration step size; $\boldsymbol{G}_n$ is the partial derivative matrix at convergence point; $\boldsymbol{C}_{\mathrm{D}}$ is the observation parameter covariance matrix; and $\boldsymbol{C}_{\mathrm{M}}$ is the covariance matrix of model parameter.

## 3 Results of uniaxial compression test

### 3.1 Tomographic inversion parameters for uniaxial compression test and wave velocity

#### 3.1.1 Uniaxial compression test and AE monitoring workflow

In the uniaxial compression test, Zigong red sandstone is selected as the study object, which is processed into a standard cylindrical specimen of 50 mm× 100 mm (diameter×height). The perpendicularity and flatness of the sample satisfy the ISRM standard[33]. The uniaxial compression test adopts the constant axial strain rate loading mode. Firstly, a 200 N preload is applied to the cylindrical sample to ensure a tight contact between loading device and sample. Load is exerted under the axial strain rate of $2.5\times10^{-6}$ $s^{-1}$ until the sample failure[4]. During loading, continuous passive AE signal acquisition and periodic active ultrasonic test are carried out simultaneously. The monitoring process is shown in Fig. 4. Eight Nano30 AE sensors are installed on the sample surface, whose operating frequency is 125–750 kHz and resonant frequency is 300 kHz. The preamplification gain of four sensors is set to 50 dB to ensure that as many microcrack signals as possible are collected during the test. The other four sensors have a preamplification gain of 30 dB so that the signals can be picked up even after severe damage. The waveform sampling rate is 10 MHz. After collecting the continuous waveform, waveform is triggered to obtain independent AE events. The threshold voltage of triggering is 0.08 V, the waveform length is 1 024 sampling points (i.e. $1.024\times10^{-4}$ s), and the minimum number of sensors is 3. After the sample is preloaded, an active ultrasonic test is carried out, and then active ultrasonic tests are performed every 300 s. Eight sensors are successively used as active sources, and the other sensors serve as receiving sensors. During active ultrasonic test, active source is simulated in the form of a sharp wave pulse. The pulse output voltage is set at 500 V, and the waveform is superimposed 25 times during pulse excitation to improve the signal-to-noise ratio (SNR). Finally, the change of ultrasonic wave velocity during loading is obtained.

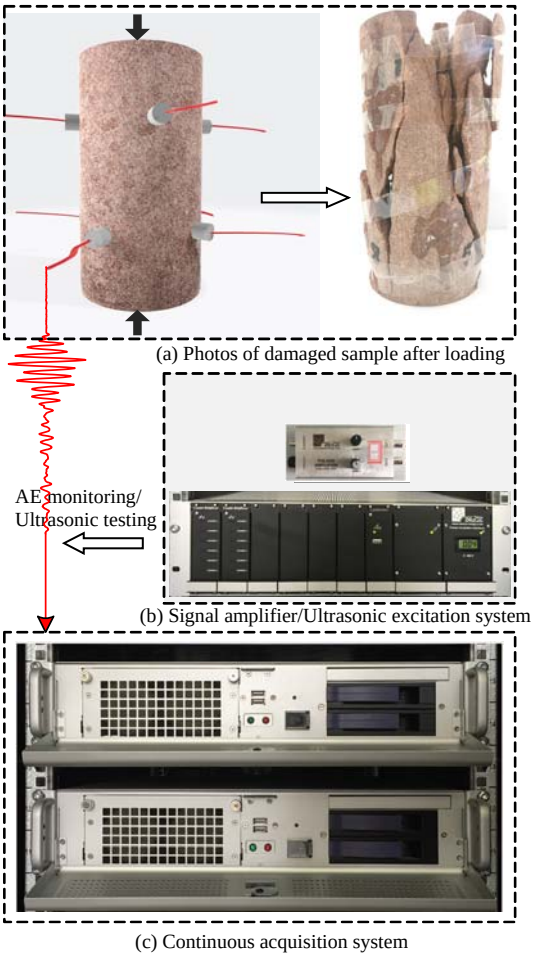


**Fig. 4 Workflow of AE monitoring during the uniaxial compression test**

#### 3.1.2 Tomographic inversion and parameters

FaATSO (fast marching acoustic emission tomography using standard optimization) is a wave velocity tomographic inversion program developed by Brantut[21], which can enable researchers to invert the P-wave velocity of rock samples by combining active ultrasonic testing and passive AE monitoring data. FaATSO program extracts the arrival time of active ultrasonic test and AE event as observation data, and use AE event coordinates, P-wave velocity and anisotropic parameter $E$ as model parameters. The anisotropic parameter is expressed as $E=(V_{\mathrm{P}}^{\mathrm{v}}-V_{\mathrm{P}}^{\mathrm{h}})/V_{\mathrm{P}}^{\mathrm{h}}$, where $V_{\mathrm{P}}^{\mathrm{v}}$ and $V_{\mathrm{P}}^{\mathrm{h}}$ are the P-wave velocities in vertical and horizontal directions, respectively. Figure 5(a) displays the workflow of tomographic inversion. The variances of the observation data and model parameters all conform to Gaussian distribution. The inversion parameters and standard deviations are summarized in Table 1. In the compression test controlled by axial loading, AE events are concentrated near the peak stage, thus the AE events are divided into a series of dataset (500 events) for wave velocity inversion. The inversion of the first two datasets is performed in combination with the ultrasonic measurement data of Survey-7 and Survey-8, respectively. Due to the lack of ultrasonic measurement data near the peak stage, the subsequent inversions are completed by AE events data. In the uniaxial compression test, a total of 12 901 AE events and two sets of ultrasonic tests (Survey-7 and Survey-8) are used for tomographic inversion. The wave velocity model results obtained from each inversion are chosen as initial wave velocity model for the next dataset inversion. A 60 mm×60 mm×100 mm grid node model is constructed based on the cylindrical model. Figure 5(b) shows the section of the grid model in vertical loading direction. The initial grid spacing is 5 mm. In order to improve the calculation accuracy, the grids are refined using trilinear interpolation, with a refined grid spacing of 1 mm. The initial P-wave velocity model is set to be transverse-isotropic. According to the active ultrasonic test results, initial P-wave velocities of the grid nodes occupied by the cylindrical sample are assigned 3.4 km/s, and the

anisotropic parameter $E$ are 0.1. The wave velocities at peripheral grid nodes are set to 0 to ensure that the elastic wave signal cannot propagate to the outside of the sample.

**Table 1 Inversion parameters used for the uniaxial compression test**

| Parameter | Arrival time of ultrasonic measurement /μs | Arrival time of AE events /μs | A priori velocity model $\sigma_{\ln V}$ | Anisotropic parameter | $x$ coordinate /mm | $y$ coordinate /mm | $z$ coordinate /mm | Step size $\lambda$ /mm |
|---|---|---|---|---|---|---|---|---|
| Standard deviation | 1 | 2 | 0.02 | 0.01 | 2 | 2 | 2 | 25 |

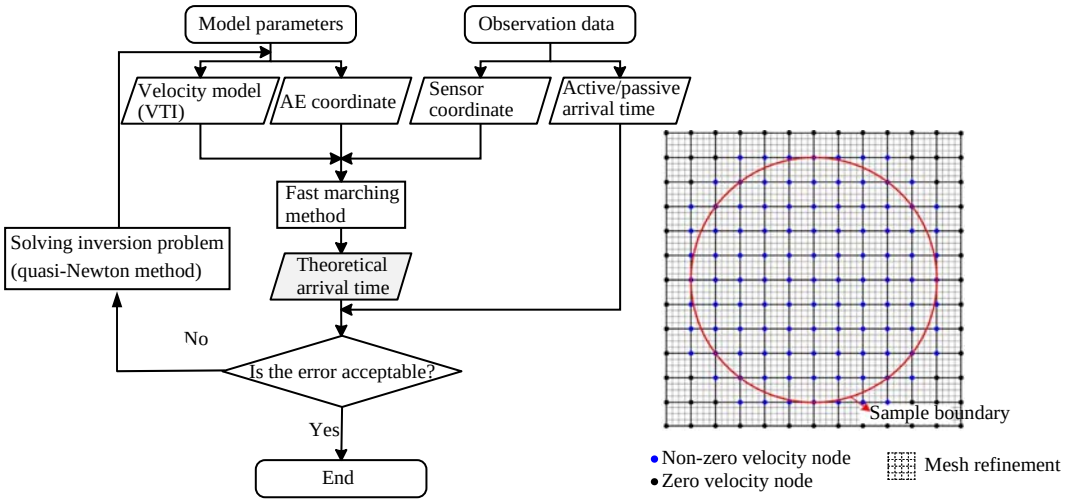


(a) Workflow of P-wave velocity inversion (b) 2D slice diagram of grid node model

**Fig. 5 Workflow of tomographic inversion and initial P-wave velocity model**

### 3.2 Mechanical test results

In this study, the uniaxial compression tests are carried out on three cylindrical samples of Zigong sandstone by constant axial strain method. Sample #1 is monitored by AE sensors while undergoing mechanical tests[4, 34]. The mechanical test results are presented in Fig. 6(a). The uniaxial compressive strengths of samples #1–#3 are 114.9, 120.7 and 100.1 MPa, and the corresponding axial strains at peak strength are $6.26\times10^{-3}$, $5.75\times10^{-3}$ and $7.04\times10^{-3}$. Figure 6(b) presents the axial stress–time curve, ultrasonic measurement and effectively located AE event rate of sample #1. Before the load peak is reached, AE event rate maintains at a low level, and the number of successfully located AE events per second is less than 10. The AE event rate reaches its maximum when the load peak is arrived, and more than 200 AE events per second are successfully located at the post-peak outbreak stage, among which up to 494 AE events per second are located at the maximum AE event rate.

### 3.3 Results of P-wave velocity tomography

Figure 7 depicts the P-wave velocity tomography and P-wave velocity difference ($V_{\text{Tomo-}i}$–$V_{\text{Tomo-}i\text{-}1}$) slices of two adjacent inversion results. The $y$-$z$ slices from the sample center are used for analysis. A total of 26 sets of inversions are performed, and then marked with Tomo-$i$ ($i$=1, 2, 3⋯) for each inversion. The AE events used in the first five tomographic inversions are located at the pre-peak stage, and the AE events used in the remaining tomographic inversions are located near the peak stage.

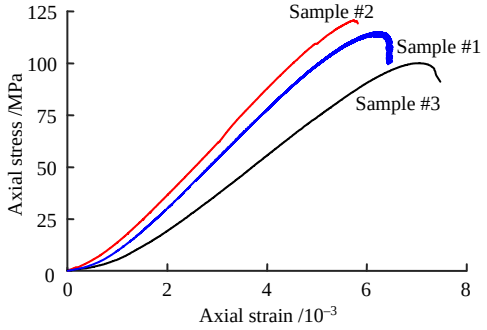


(a) Uniaxial compression stress–strain curve of Zigong sandstone under axial strain-controlled loading

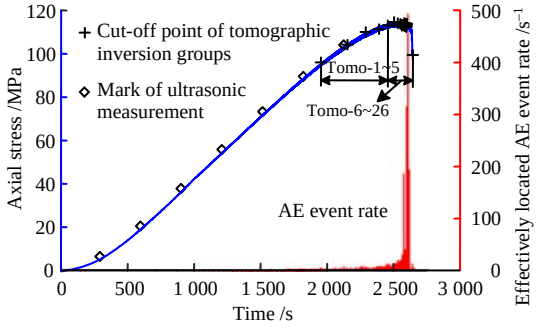


(b) Ultrasonic measurement and effectively located AE event rate of sample #1

**Fig. 6 Stress–strain curves of the Zigong sandstone in uniaxial compression tests**

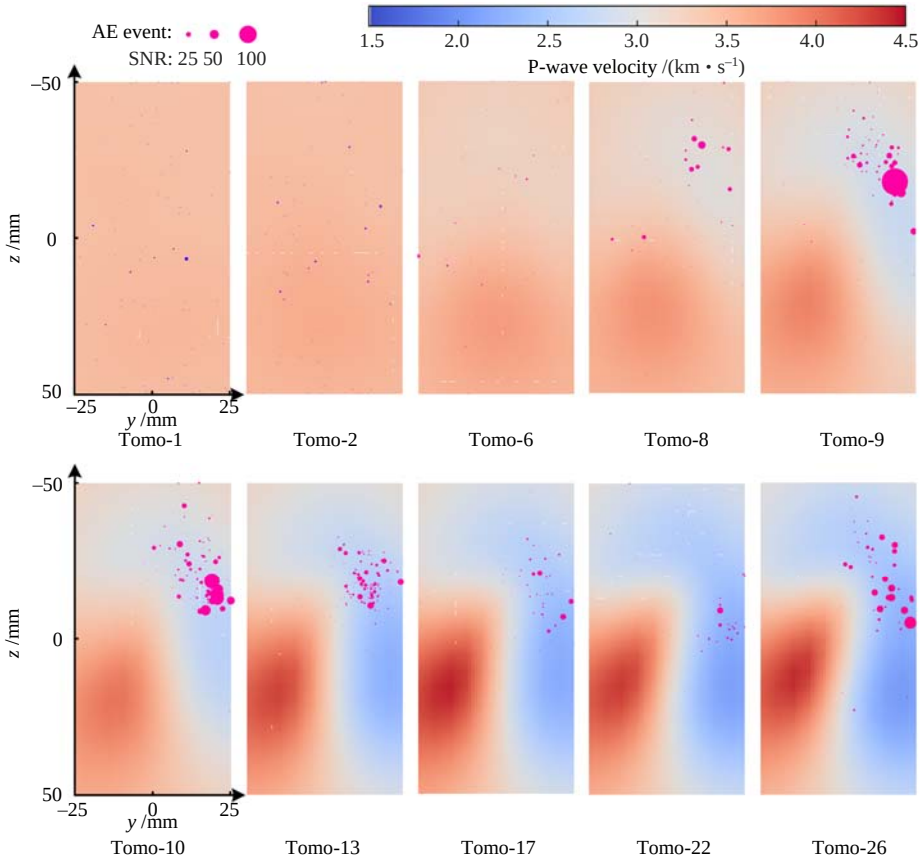


(a) P-wave velocity and AE event location (AE event refers to the collection of AE events located in the area perpendicular to the slice within the space range of ±5 mm)

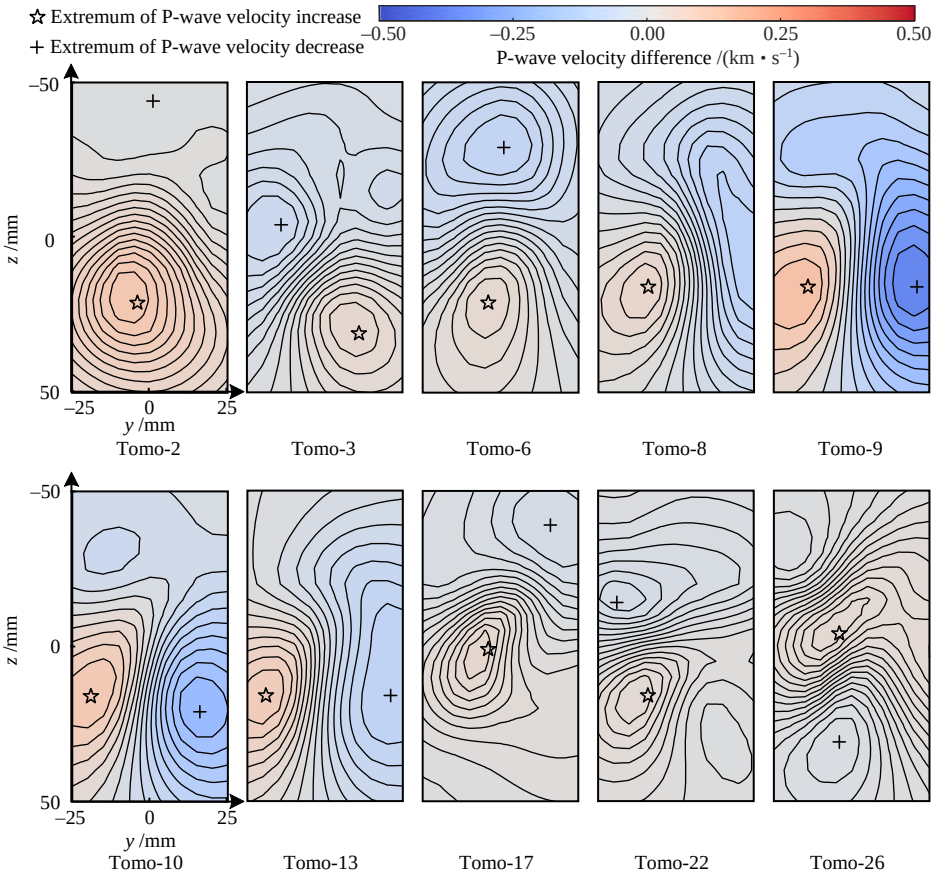


(b) Contour maps showing P-wave velocity difference between two adjacent inversions

**Fig. 7 Results of P-wave tomographic inversion and P-wave velocity changes of the sample under loading**

The contour maps in Fig. 7(a) display the evolution of P-wave velocity and AE events location results. From blue to red, P-wave velocity gradually increases, and the wave velocity is in the range of 1.5–4.5 km/s. The AE events in the tomographic view are the projections of AE events located in the area perpendicular to the slice within the space range of ±5 mm, and the size of the solid circle denotes the SNR of AE events. The AE data used in Tomo-1 and Tomo-2 inversions are all located at the pre-peak stage, and the obtained P-wave velocity change is not obvious. The minimum P-wave velocity $V_{\min}$ in the slice is 3.40–3.41 km/s, and there is no significant change from the initial wave velocity of 3.40 km/s. The maximum P-wave velocity $V_{\max}$ falls in the range of 3.51–3.61 km/s. AE events are randomly distributed in space, with low SNR of successfully located events. The AE events used in Tomo-6 inversion appear near the peak. The wave velocity increases in the bottom area, reaching the maximum of 3.73 km/s. According to the Tomo-8 inversion, there is a low velocity region in the upper right corner of *y*-*z* slice, where AE events are concentrated. The minimum wave velocity in this low-velocity region is 3.03 km/s. According to the velocity field evolution in Tomo-9–Tomo-13, the range of low velocity region on the right side continues to increase with loading, and $V_{\min}$ drops from 2.78 km/s to 2.25 km/s, decreasing by 19.0%. AE events occur in the same location as in the low wave velocity region, appearing inside the low velocity region and concentrated in the upper part of the sample. Furthermore, among the successfully located events, high SNR events emerge, and the heterogeneity of the sample becomes prominent with ongoing loading. After Tomo-13 inversion, high velocity region is formed in the lower left part. In the meantime, low velocity region on the right continues to expand, and the top area also changes into low velocity region. However, at this stage, the minimum wave velocity does not change significantly, and AE events still cluster in the upper right and inside the low velocity region.

Figure 7(b) shows the contour map of P-wave velocity difference between the two adjacent inversions. Blue means a decreasing trend of wave velocity, while red denotes an increasing trend. Star represents the extremum of increasing wave velocity, and the plus sign represents the extremum of decreasing wave velocity. Compared with Tomo-1, P-wave velocity of Tomo-2 experiences an overall increase, and the maximum increase occurs at the bottom. Starting from Tomo-3, P-wave velocity in the upper part of the sample undergoes a downward trend, and this situation continues until Tomo-6, indicating that the sample has been damaged at the pre-peak stage. Between Tomo-8 and Tomo-13 inversions, the region of rising wave velocity appears in the lower right, while the region of decreasing wave velocity is encountered in the right half and the top of the sample. The wave velocities of Tomo-9 and Tomo-10 inversions decrease significantly by 357.1 m/s and 208.1 m/s respectively. In the subsequent inversions (Tomo-17, Tomo-22 and Tomo-26), the velocity difference varies within a marginal range, and the extrema of velocity decrease and increase are both less than 100 m/s, which are consistent with P-wave velocity and distribution shown in Fig. 7(a).

An obvious low velocity region has been observed in Tomo-9 inversion, during which AE events gather. However, from the contour map of wave velocity difference in Fig. 7(b), P-wave velocity in some areas begin to decrease from Tomo-3, and the amplitude of reduction of Tomo-9 hits the peak. The decreasing trend of P-wave velocity at the pre-peak stage indicates the damage at this stage.

### 3.4 Evolution of P-wave dispersion

In previous analysis, P-wave velocity variation is mostly based on the average ray path, which is difficult to characterize the local changes in the sample. In addition, ray path can hardly cover the whole sample, and thus is incapable of reflecting the characteristics of wave velocity change. To address this issue, P-wave dispersion[35] was proposed to represent the non-uniformity of wave velocity distribution during inversion, which is defined as the difference between the maximum and minimum P-wave velocities.

Figure 8 presents the changes of wave velocity using active ultrasonic technology under two characteristic paths, the changes of maximum and minimum in the wave velocity inversion model, and the evolution of P-wave velocity dispersion with time. The leftwards and rightwards triangles in Fig. 8 represent the average wave velocities $V_{\text{S4-S5}}$ and $V_{\text{S1-S3}}$ corresponding to paths S4-S5 and S1-S3, respectively. P-wave velocity along the loading axis $V_{\text{S4-S5}}$ is larger than that perpendicular to the loading axis $V_{\text{S1-S3}}$. $V_{\text{S4-S5}}$ reaches the maximum wave velocity of 3.88 km/s in the 7th ultrasonic test (78.0% peak strength), while $V_{\text{S1-S3}}$ reaches the maximum wave velocity of 3.47 km/s in the 5th ultrasonic test (48.0% peak strength). Since no active ultrasonic test is conducted near the peak stage, the wave velocity change at the peak based on active ultrasonic test is unavailable. In tomographic inversion, 500 AE events are bound into a group, in order to probe into the wave velocity evolution law around the peak strength. In Fig. 8, the inverted and regular triangles indicate the maximum and minimum wave velocities, $V_{\max}$ and $V_{\min}$, calculated by tomographic inversion, and the blue circle marks the P-wave dispersion $V_{\text{disp}}$. At the pre-peak stage (Tomo-1–Tomo-5), there are no significant changes in $V_{\max}$ and $V_{\min}$. The slope of $V_{\text{disp}}$ is small, rising from 0.11 km/s to 0.51 km/s. In stark contrast, after Tomo-9 (near the peak stage), $V_{\max}$ and $V_{\min}$ change drastically, and the slope of the dispersion curve increases. At Tomo-9, $V_{\text{disp}}$ climbs to 1.55 km/s, which is 64.9% higher than that of Tomo-8 (0.94 km/s), and goes up continuously in

subsequent inversions until failure occurs. At Tomo-25, $V_{max}$ and $V_{min}$ are 4.43 km/s and 1.48 km/s, respectively, and $V_{disp}$ is 2.95 km/s. $V_{diff}$ is defined as the extremum of velocity reduction from two inversion results, noted by plus sign in Fig. 7(b) and blue rectangle in Fig. 8. At Tomo-9, $V_{diff}$ reaches the peak of 0.52 km/s, and most inversion results show that the single wave velocity difference is less than 0.1 km/s.

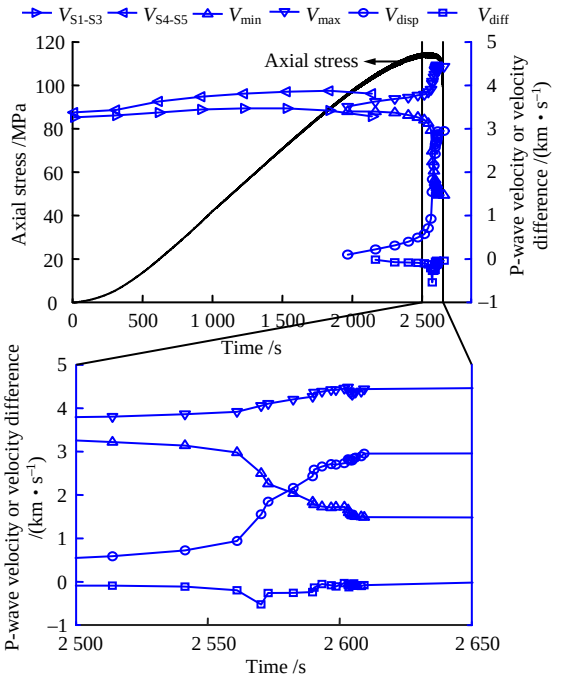


**Fig.8 P-wave velocity and dispersion of P-wave velocity**

### 3.5 AE location results

In this study, the heterogeneous velocity model is used to locate AE events. The AE location algorithm adopted is the source location method based on the arrival time difference database. The specific implementation is described below:

(1) The sample is first discretized into a grid node model, and then the heterogeneous wave velocity model is built based on sensor position coordinates and tomographic inversion in Section 3.3. This heterogeneous wave velocity model is used to output the theoretical arrival time of each grid node through forward calculation, and then the theoretical arrival time difference matrix of any two sensors is obtained.

(2) For any AE event recorded in the test, the arrival time information of the waveform signal to the sensor is extracted, and the real arrival time difference between any two sensors is calculated.

(3) The real time difference and theoretical arrival time difference matrix are matched and searched for any AE sensor, and the minimum L1 norm of the real and theoretical arrival time difference is regarded as the source location. The influence of homogeneous and heterogeneous velocity models on location results will be discussed in detail in Section 4.1.

The location results of the uniaxial compression test on sandstone are shown in Fig. 9, where the SNR is represented by the magnitude of AE events. The test stage is divided in terms of peak strength, and the three-view drawings and 3D maps (bottom right corner) of AE events location at different stages are demonstrated. In Fig. 9(a), AE events occur at random locations at the pre-peak stage, uniformly distributed in the sample, and no high SNR events are detected. At the initial loading stage, AE events are less developed, mostly appearing near the peak. At the post-peak stage, the locations of AE events are relatively concentrated near the peak (Fig. 9(b)). According to the *x*-*y* and *y*-*z* views, AE events are concentrated in the top left corner, with many high SNR events being successfully located. The massive emergence of AE events near the peak promotes the initiation, propagation and coalesce of cracks, and eventually induces the macro-failure of the sample. In the uniaxial compression test, AE events are clustered on sandstone surface, which is consistent with the hourglass-shaped failure found in field observations[36–37] and numerical simulation[9].

## 4 Discussion

### 4.1 Location errors of different velocity models

AE monitoring is widely used to study the evolution of rock failure. It explains the initiation and fracture of microcracks in rock from a microscopic perspective by locating AE events. AE location accuracy is affected by arrival time pickup, velocity model and location algorithm selection[38–41]. In order to explore the influence of velocity model on location results, the source location method based on arrival time database introduced in Section 3.5 is adopted to study the location accuracy in homogeneous and heterogeneous velocity models. Firstly, a 2D heterogeneous anisotropic disk is defined, whose P-wave velocity value is generated by peaks function and presents a binary Gaussian distribution in space ( $V_p$ =1.7–4.6 km/s). The anisotropy axis is the *z* axis, and the anisotropy parameter *E* is equal to 0.1. Fifty sources are randomly generated inside the disk (Fig. 10(a)). FMM is then used in forward calculation to obtain the arrival time of each source to the sensor on disk surface. According to the arrival time in the homogeneous velocity model, the source coordinates are solved (Fig. 10(b)), and then the error is estimated by comparing the location results in homogeneous model with actual source locations. Source locations in the heterogeneous velocity model are the real coordinates. Location error can be defined as the distance of the location results of the same source in the heterogeneous and homogeneous velocity models, and the ratio of source to the minimum disk size is defined as relative error. Figure 10(c) shows the relative error distribution of artificial sources. The statistical results of 26 sources suggest that the relative error of more than half of the location results is greater than 5% when using the simplified homogeneous velocity model. Among them, the relative location errors of two sources are beyond 10%, and the

maximum error reaches up to 12.5%, corresponding to the location distance deviation of 6.2 mm. The relative errors of most source locations are about 5%.

Figure 10 reveals that the simplified homogeneous velocity model will bring about certain errors when applied to source location. Figure 11 compares the relative errors of AE event location results using homogeneous and heterogeneous velocity models in the uniaxial compression test on cylindrical sandstone. In the homogeneous velocity model, the wave velocity is set at 3.4 km/s, independent of the load. The heterogeneous velocity model is established from the integrated tomographic inversion of active ultrasonic data and AE events.

Figure 11(a) shows the evolution of relative location error over time. At the pre-peak stage (Tomo-1–Tomo-5), both the relative errors of the homogeneous and heterogeneous models fluctuate within a lower level, ranging from 6.1% to 7.8%. A large number of AE events are effectively located near the peak stage, and the relative errors of two velocity models experience an increasing trend, with the maximum error close to 20%. The duration of this stage is relatively short, but the sharp increase of location error indicates a noticeable velocity differentiation, which is consistent with the results of velocity model inversion

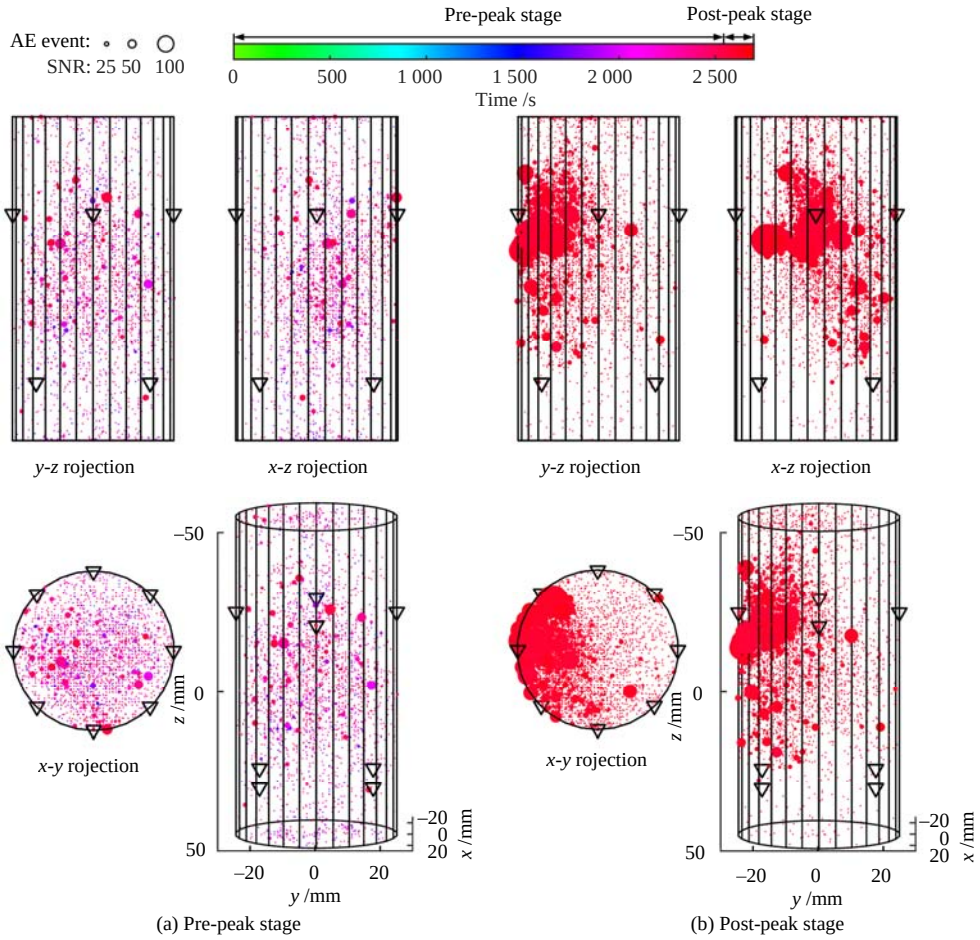


**Fig. 9 AE locations shown in three projections of the sandstone sample during the pre-peak and post-peak stages**

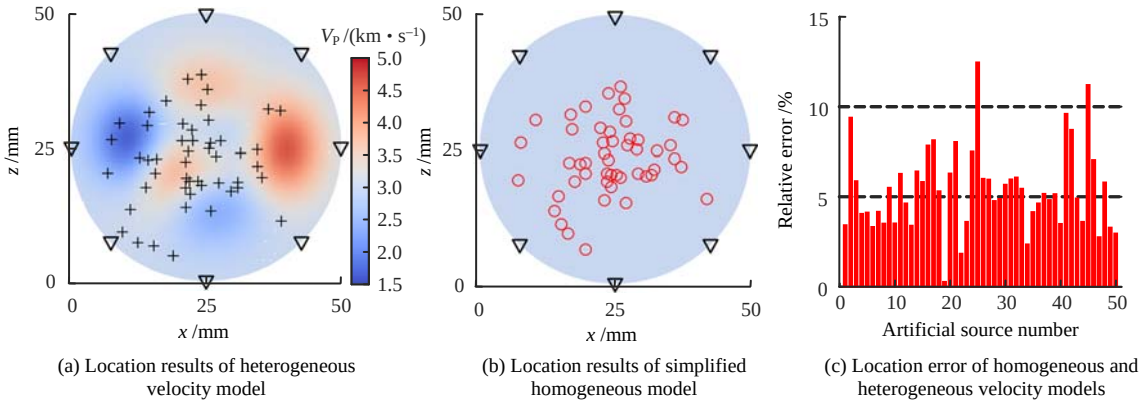


**Fig. 10 Comparison of AE locations between homogeneous and heterogeneous velocity structures**

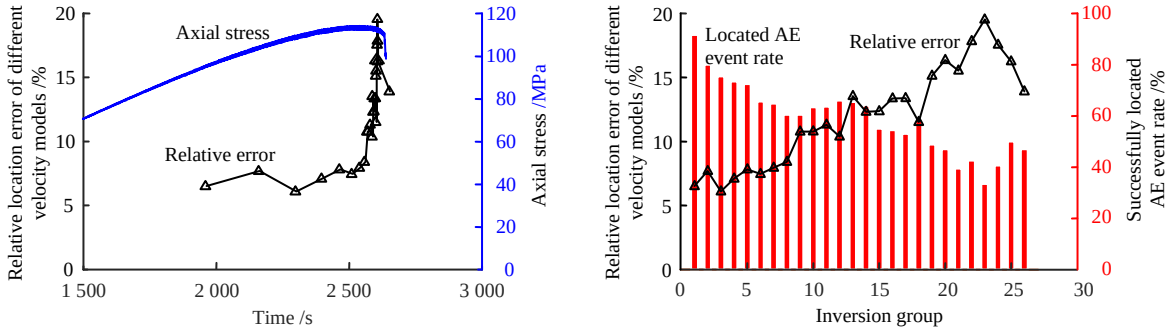


(a) Evolution law of location error–time (b) Relationship between location error and inversion group

**Fig. 11 Relative location errors between the homogeneous and heterogeneous velocity structures in the uniaxial compression test**

shown in Fig. 7. Figure 11(b) displays the relationship between relative location error and inversion group, as well as the successfully located AE event rate. Note that each group contains 500 AE events. The relative location error increases gradually near the peak, but decreases from 19.5% to 13.9% in the last four inversions. The red bar chart shows the proportion of AE events successfully located in each inversion group. In the first inversion, 91.6% of AE events are located. Successful location rate decreases with loading. From Tomo-8 to Tomo-13, successful location rate slightly increases from 60% to 65%, but the overall trend is decreasing. The minimum successful location rate of 33.4% appears at Tomo-23, where the relative location errors of two velocity models reach the maximum.

### 4.2 Variation of *b* value

Gutenberg et al.[42] proposed a relationship between seismic magnitude and frequency, i.e. the Gutenberg-Richter's (G-R) law:

$$\lg N = a - bM \tag{12}$$

where $N$ is the event frequency greater than magnitude $M$; $M$ is the magnitude of seismic activity; and $a$ and $b$ are the constants.

Numerous scholars[43–46] have found that the statistical behavior of fracture activity observed in laboratory is similar to that of seismic activity, showing consistency not only in the magnitude–frequency relationship, but also in the pre-fracture activity accumulation and pre-seismic sequence. In this paper, the maximum likelihood method[47–49] is used to calculate the $b$ value. To eliminate errors caused by too few AE events within a certain magnitude range, the length of AE event calculation time window is set as 1 000, and the sliding step of time window is set as 300. The $b$ value changing with the location event is calculated, and the variation of $b$ value with loading time is obtained.

Figure 12 plots the change of $b$ value over time in uniaxial compression test. The $b$ value is highlighted by black circle, whose error distribution is represented by gray shadow. The calculated $b$ value of the first 1 000 AE events is 2.61. At the pre-peak stage, with the increase in load, $b$ value increases first and then decreases, remaining at a relatively high level (2.61–2.91). At this stage, low magnitude events occupy a high proportion where small-scale fracture is dominant. Near the peak, stress maintains a high level with a $b$ value of 2.43. At the post-peak stage, $b$ value undergoes a rapid downward trend and hits the bottom of 1.09 before the final failure. The rapid decline of $b$ value indicates that a large number of high-magnitude events occur before the sample failure. This finding is in accordance with the rule found in the studies of hornblende, granite, marble and sandstone by Lei[50] and Li et al.[51], which confirms that before the final failure, high-magnitude events increase while the $b$ value decreases. In addition, the decrease of $b$ value also indicates that large-scale cracks form before the macro-failure, leading to the increase of rock heterogeneity, which further proves the necessity of using the time-varying heterogeneous velocity model for AE source location.

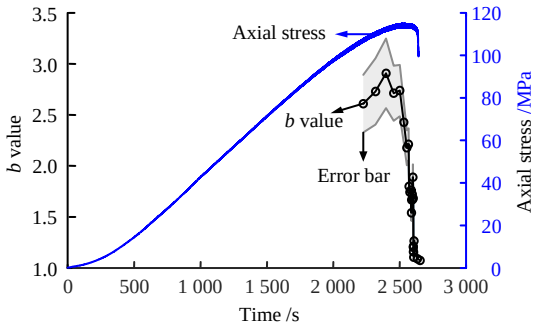


**Fig. 12 Variation of *b* value in the uniaxial compression test on sandstone**

## 5 Conclusions

In this study, the damage and fracture of sandstone under uniaxial compression are studied by active ultrasonic measurement and passive AE monitoring. A 3D time-varying wave velocity model is proposed by using the integrated inversion technology of active ultrasonic measurement and passive AE monitoring. Then the heterogeneous wave velocity model obtained by inversion is applied to AE events source location to improve the location accuracy. The main conclusions are drawn as follows:

(1) P-wave velocity tomography results show that under loading, low-velocity region will first appear at the end of sample, and gradually expand inward with loading. The P-wave velocity difference in the adjacent inversions suggests that the extremum of velocity reduction appears at the end of the sample before the peak, while the extremum of velocity reduction occurs randomly near the peak both at the end of and inside the sample.

(2) Before the load peak is reached, AE events are distributed randomly in the sample, without high SNR events being successfully located. At this stage, no obvious low-velocity region appears in wave velocity tomography. At the post-peak stage, as the rock breaks, AE signals are released and P-wave velocity decreases. Near the peak, AE events are clustered on one side of the sample, and AE sources are located in the low-velocity region from the tomography results.

(3) The maximum and minimum of wave velocities obtained by P-wave velocity tomographic inversion vary dramatically near the peak. P-wave dispersion increases the most at the peak in Tomo-9, and continues to grow in the subsequent inversions.

(4) It is found that the location error will be introduced when applying homogeneous velocity model for AE source location. The relative location errors calculated by the homogeneous and heterogeneous velocity models are compared. At the pre-peak stage, the relative error of the homogeneous model is small. A swarm of AE events are successfully located near the peak, indicating an intensified microcrack activity and sample heterogeneity. Therefore, the relative location error increases, and the maximum relative error is close to 20%.

## References

[1] XU Y H, CAI M. Influence of strain energy released from a test machine on rock failure process[J]. Canadian Geotechnical Journal, 2018, 55(6): 777–791.

[2] REED G, MCTYER K, FRITH R. An assessment of coal pillar system stability criteria based on a mechanistic evaluation of the interaction between coal pillars and the overburden[J]. International Journal of Mining Science and Technology, 2017, 27(1): 9–15.

[3] HUDSON J A, CROUCH S L, FAIRHURST C. Soft, stiff and servo-controlled testing machines: a review with reference to rock failure[J]. Engineering Geology, 1972, 6(3): 155–189.

[4] ZHANG S, WU S, CHU C, et al. Acoustic emission associated with self-sustaining failure in low-porosity sandstone under uniaxial compression[J]. Rock Mechanics and Rock Engineering, 2019, 52(7): 2067– 2085.

[5] WANG J A, SHANG X C, MA H T. Investigation of catastrophic ground collapse in Xingtai gypsum mines in China[J]. International Journal of Rock Mechanics and Mining Sciences, 2008, 45(8): 1480–1499.

[6] DONG H, ZHU W, HOU C, et al. Load transfer behavior during cascading pillar failure: an experimental study[J]. Rock Mechanics and Rock Engineering, 2022, 55(3): 1445–1460.

[7] GILL D E, AUBERTIN M, SIMON R. A practical engineering approach to the evaluation of rockburst potential[C]//Rockburst and Seismicity in Mines. Rotterdam: Balkema, 1993: 63–68.

[8] LI G, CHENG X, HU L, et al. Rock failure and instability from a structural perspective: insights from the shape effect[J]. Rock Mechanics and Rock Engineering, 2022, 55(2): 937–952.

[9] RENANI R H, MARTIN C D. Modeling the progressive failure of hard rock pillars[J]. Tunnelling and Underground Space Technology, 2018, 74: 71–81.

[10] WANG S Y, LAM K C, AU S K, et al. Analytical and numerical study on the pillar rockbursts mechanism[J]. Rock Mechanics and Rock Engineering, 2006, 39(5): 445–467.

[11] YAO Xu-long, ZHANG Yan-bo, LIU Xiang-xin, et al. Optimization method for key characteristic signal of acoustic emission in rock fracture[J]. Rock and Soil Mechanics, 2018, 39(1): 375–384.

[12] ZHANG Yan-bo, XU Yue-dong, LIU Xiang-xin, et al. Quantitative characterization and mesoscopic study of propagation and evolution of three-dimensional rock fractures based on CT[J]. Rock and Soil Mechanics, 2021, 42(10): 2659–2671.

[13] SUN Wen-jin, JIN Ai-bing, WANG Shu-liang, et al. Study on sandstone split mechanical properties under high temperature based on the DIC technology[J]. Rock and Soil Mechanics, 2021, 42(2): 511–518.

[14] HE M C, ZHAO F, CAI M, et al. A novel experimental technique to simulate pillar burst in laboratory[J]. Rock Mechanics and Rock Engineering, 2015, 48(5): 1833–1848.

[15] CHEN Guo-qing, LI Yang, CHEN Ya-feng, et al. Thermal-acoustic sensitivity analysis of fractured rock with different lithologies[J]. Chinese Journal of Rock Mechanics and Engineering, 2022, 41(10): 1945–1957.

[16] GOODFELLOW S D, TISATO N, GHOFRANITABARI M, et al. Attenuation properties of Fontainebleau

sandstone during true-triaxial deformation using active and passive ultrasonics[J]. Rock Mechanics and Rock Engineering, 2015, 48(6): 2551–2566.

[17] YUKUTAKE H. Fracturing process of granite inferred from measurements of spatial and temporal variations in velocity during triaxial deformations[J]. Journal of Geophysical Research, 1989, 94(B11): 15639–15651.

[18] MEGLIS I L, CHOW T, MARTIN C D, et al. Assessing in situ microcrack damage using ultrasonic velocity tomography[J]. International Journal of Rock Mechanics and Mining Sciences, 2005, 42(1): 25–34.

[19] FALLS S D, YOUNG R P, CARLSON S R, et al. Ultrasonic tomography and acoustic emission in hydraulically fractured Lac du Bonnet grey granite[J]. Journal of Geophysical Research, 1992, 97(B5): 6867–6884.

[20] JANSEN D P, CARLSON S R, YOUNG R P, et al. Ultrasonic imaging and acoustic emission monitoring of thermally induced microcracks in Lac du Bonnet granite[J]. Journal of Geophysical Research: Solid Earth, 1993, 98(B12): 22231–22243.

[21] BRANTUT N. Time-resolved tomography using acoustic emissions in the laboratory, and application to sandstone compaction[J]. Geophysical Journal International, 2018, 213(3): 2177–2192.

[22] VIDALE J. Finite-difference calculation of travel times[J]. Bulletin of the Seismological Society of America, 1988, 78(6): 2062–2076.

[23] VIDALE J. Finite-difference calculation of traveltimes in three dimensions[J]. Geophysics, 1990, 55(5): 521–526.

[24] XU Yang. Research on tomography inversion based on fast marching method[D]. Beijing: China University of Petroleum-Beijing, 2017.

[25] RAWLINSON N, SAMBRIDGE M. Wave front evolution in strongly heterogeneous layered media using the fast marching method[J]. Geophysical Journal International, 2004, 156(3): 631–647.

[26] JIANG Ruo-chen, XU Nu-wen, DAI Feng, et al. Research on microseismic location based on fast marching upwind linear interpolation method[J]. Rock and Soil Mechanics, 2019, 40(9): 3697–3708.

[27] SETHIAN J A, POPOVICI A M. 3-D traveltime computation using the fast marching method[J]. Geophysics, 1999, 64(2): 516–523.

[28] RICKETT J, FOMEL S. A second-order fast marching eikonal solver[R]. Stanford, CA: Stanford University, 2000: 287–292.

[29] ZHANG Kai, CHEN Jun-yi, ZHU Bai-hang, et al. First break traveltime tomographic imaging based on the eikonal equation in VTI medium[J]. Oil Geophysical Prospecting, 2018, 53(6): 1218–1226.

[30] SETHIAN J A. Fast marching methods[J]. SIAM Review, 1999, 41(2): 199–235.

[31] LI Qiang. Seismic traveltime tomography by using a fast marching method based on solving eikonal equation[D]. Xi'an: Chang'an University, 2012.

[32] TARANTOLA A. Inverse problem theory and methods for model parameter estimation[M]. Philadelphia: Society for Industrial and Applied Mathematics, 2004.

[33] ULUSAY R. The ISRM suggested methods for rock characterization, testing and monitoring: 2007-2014[S]. Switzerland: Springer International Publishing, 2015.

[34] ZHANG Shi-huai. Study on strength and deformability of hard brittle sandstone[D]. Beijing: University of Science and Technology Beijing, 2019.

[35] CHEN Yong, YANG Xian-wu, HAN Biao. Spatial velocity variations of P waves during rock deformations[J]. Acta Geophysica Sinica, 1990, 12(1): 54–59.

[36] PRITCHARD C J, HEDLEY D G F. Progressive pillar failure and rockbursting at Denison mine[C]//Proceedings of 3rd International Symposium on Rockbursts and Seismicity in Mines. Rotterdam: Balkema, 1993: 111J6.

[37] WAGNER H. Determination of the complete load-deformation characteristics of coal pillars[C]// Proceedings of the 3rd International Congress on Rock Mechanics. Denver: [s. n.], 1974: 1076–1081.

[38] LI Xiang, XU Nu-wen. Research developments and prospects on microseismic source location[J]. Progress in Geophysics, 2020, 35(2): 598–607.

[39] DONG Long-jun, LI Xi-bing, TANG Li-zhong. Main influencing factors for the accuracy of microseismic source location[J]. Science & Technology Review, 2013, 31(24): 26–32.

[40] LIU Jian-po, WANG Hong-yong, YANG Yu-jiang, et al. Experimental study on different rock locating algorithms with acoustic emission[J]. Journal of Northeastern University(Natural Science), 2009, 30(8): 1193–1196.

[41] WU Shun-chuan, GUO Chao, GAO Yong-tao, et al. Discussion and prospect of source location of rock fracture[J]. Chinese Journal of Rock Mechanics and

Engineering, 2021, 40(5): 874–891.

[42] GUTENBERG B, RICHTER C F. Frequency of earthquakes in California[J]. Bulletin of the Seismological society of America, 1944, 34(4): 185–188.

[43] SCHOLZ C H. The frequency-magnitude relation of microfracturing in rock and its relation to earthquakes[J]. Bulletin of the Seismological Society of America, 1968, 58(1): 399–415.

[44] SCHOLZ C H. Microfractures, aftershocks, and seismicity[J]. Bulletin of the Seismological Society of America, 1968, 58(3): 1117–1130.

[45] GUO P, WU S, ZHANG G, et al. Effects of thermally-induced cracks on acoustic emission characteristics of granite under tensile conditions[J]. International Journal of Rock Mechanics and Mining Sciences, 2021, 144: 104820.

[46] LEI X, MA S. Laboratory acoustic emission study for earthquake generation process[J]. Earthquake Science, 2014, 27(6): 627–646.

[47] WIEMER S, WYSS M. Minimum magnitude of completeness in earthquake catalogs: examples from Alaska, the Western United States, and Japan[J]. Bulletin of the Seismological Society of America, 2000, 90(4): 859–869.

[48] SCHULTZ R, ATKINSON G, EATON D W, et al. Hydraulic fracturing volume is associated with induced earthquake productivity in the Duvernay play[J]. Science, 2018, 359(6373): 304–308.

[49] MARZOCCHI W, SANDRI L. A review and new insights on the estimation of the *b*-value and its uncertainty[J]. Annals of Geophysics, 2003, 46(6): 1271–1282.

[50] LEI X, KUSUNOSE K, RAO M V M S, et al. Quasi-static fault growth and cracking in homogeneous brittle rock under triaxial compression using acoustic emission monitoring[J]. Journal of Geophysical Research: Solid Earth, 2000, 105(3): 6127–6139.

[51] LI Yuan-hui, LIU Jian-po, ZHAO Xing-dong, et al. Study on *b*-value and fractal dimension of acoustic emission during rock failure process[J]. Rock and Soil Mechanics, 2009, 30(9): 2559–2563, 2574.